catalysts

MDPI

Article

Plasmonic Bi-Modified $Bi_2Sn_2O_7$ Nanosheets for Efficient Photocatalytic NO Removal

Ning Li [1,2,3,*], Wenwen Zhao [2], Jiatong Zhang [2], Xuhui Liu [2], Yangqin Gao [2] and Lei Ge [1,2,*]

[1] Key Laboratory of Heavy Oil Processing, China University of Petroleum Beijing, No. 18 Fuxue RD, Beijing 102249, China
[2] Department of Materials Science and Engineering, College of New Energy and Material, China University of Petroleum Beijing, No. 18 Fuxue RD, Beijing 102249, China
[3] Beijing Key Laboratory of Failure, Corrosion, and Protection of Oil/Gas Facilities, Beijing 102249, China
* Correspondence: lining@cup.edu.cn (N.L.); gelei@cup.edu.cn (L.G.)

Abstract: The photocatalytic removal of nitric oxide (NO) is a promising technology used to reduce the level of harmful gaseous pollutants in parts per billion (ppb). As a potential photocatalyst, $Bi_2Sn_2O_7$ has a low quantum efficiency due to its fast recombination rate of photo-generated carriers. In this paper, $Bi/Bi_2Sn_2O_7$ was prepared by the in situ deposition of Bi. The structural, electrical, and optical properties of the attained sample were investigated through a series of analyses. The results demonstrate that Bi nanoparticles not only enhance the photoabsorption ability of $Bi_2Sn_2O_7$ due to their surface plasmon resonance (SPR) effect, but also improve its photocatalytic activity. Photocatalytic performance was evaluated by the oxidation of NO at ppb level under xenon lamp ($\lambda > 400$ nm) irradiation. It was found that the photocatalytic NO removal rate increased from 7.2% ($Bi_2Sn_2O_7$) to 38.6% ($Bi/Bi_2Sn_2O_7$). The loading of Bi promotes the separation and migration of photo-generated carriers and enhances the generation of $\bullet O^{2-}$ and •OH radicals responsible for the oxidation of NO. The $Bi/Bi_2Sn_2O_7$ composite photocatalyst also exhibits excellent photocatalytic stability, which makes it a potential candidate for use in air purification systems.

Keywords: $Bi/Bi_2Sn_2O_7$; photocatalytic NO activity; SPR effect of Bi

Citation: Li, N.; Zhao, W.; Zhang, J.; Liu, X.; Gao, Y.; Ge, L. Plasmonic Bi-Modified $Bi_2Sn_2O_7$ Nanosheets for Efficient Photocatalytic NO Removal. *Catalysts* **2024**, *14*, 275. https://doi.org/10.3390/catal14040275

Academic Editor: Vasile I. Parvulescu

Received: 15 March 2024
Revised: 3 April 2024
Accepted: 12 April 2024
Published: 18 April 2024

1. Introduction

Along with the rapid development of the economy and continuous use of energy, environmental pollution and resource shortages have become very challenging problems. One of the harmful gaseous pollutants produced by the combustion of fossil fuels is NO, which not only causes acid rain but also affects the human respiratory system [1–3]. Currently, industrial treatment methods for NO_x primarily include selective catalytic reduction (SCR) and selective non-catalytic reduction (SNCR) [4]. However, these techniques only have a removal effect at high NO_x concentrations and high temperatures, and the removal efficiency at low concentrations of ppb grade NO_x is lacking. In addition, the equipment is expensive and can easily cause secondary pollution. Therefore, there is an urgent need to develop efficient and environmentally friendly methods for removing low NO_x concentrations.

Semiconductor photocatalysts have attracted wide-ranging attention because of their applications in solving environmental pollution and energy crisis. The removal of nitrogen oxide (NO) through visible light-driven photocatalysis offers several advantages, including a low cost, high efficiency at room temperature, and environmental friendliness. This method is particularly effective for removing NO at low concentrations in the ppb range [5]. When the photocatalytic material is exposed to light of the appropriate wavelength, the electrons and holes generated undergo oxidation–reduction reactions with O_2 and H_2O adsorbed on the surface. This process produces reactive oxygen species (ROS), such as superoxide radicals ($\bullet O_2^-$) and hydroxyl radicals (•OH), which play a crucial role in breaking NO_x in the air [6]. The photocatalytic removal of NO_x can result in the production of the toxic intermediate NO_2,

which is more harmful than NO and can lead to secondary pollution. Therefore, preventing the formation of NO_2 is also a crucial concern in photocatalytic NO conversion.

The layer structure of bismuth-based photocatalysts is unique, allowing for the formation of a strong built-in electric field within the crystal. This improves the separation of the photogenerated supports, resulting in excellent photocatalytic performance [7]. Therefore, several bismuth-based photocatalysts have garnered attention in the field of photocatalytic NO removal, such as $BiVO_4$ [8], Bi_2WO_6 [9], and Bi_2MoO_6 [10]. For example, Wang et al. successfully prepared a layered $Bi_2O_2CO_3$/g-C_3N_4 heterojunction photocatalyst using a one-pot hydrothermal method, which had the highest NO removal rate of 34.8% under visible light irradiation, showing high stability and durability [11]. Liao et al. constructed OVs on the surface of BiOCl to regulate the transfer of photogenerated carriers on the surface, improve the photocatalytic conversion of NO and effectively control the generation rate of NO_2 [12]. Among these Bi-based photocatalyst, pyrochlore-type $Bi_2Sn_2O_7$ with a suitable E_g of about 2.78 eV has attracted much attention due to its unique crystal structure, electronic structure, and good photocatalytic performance [13,14]. However, the severe charge recombination on the surfaces of $Bi_2Sn_2O_7$ is not conducive to their application in photocatalysis [15,16]. Currently, $Bi_2Sn_2O_7$-based heterostructures have been exploited to obtain enhanced light absorption, efficient charge separation and transport, and improved stability [17]. Li et al. investigated the photocatalytic splitting of water to produce hydrogen using the Bi@$Bi_2Sn_2O_7$/TiO_2 system [18]. $Bi_2Sn_2O_7$ grows on the surface of TiO_2 to form p-n heterojunctions to enhance the separation of photogenerated electron–hole pairs, which improves the photocatalytic activity of the system. Zhang et al. synthesized $Bi_2Sn_2O_7$ quantum dots using a solvothermal method to achieve the band structure adjustment and enhance the activation of molecular nitrogen [19]. Due to the combined effect of quantum dots and oxygen vacancies, the system has excellent photocatalytic nitrogen fixation performance. SnO_2/$Bi_2Sn_2O_7$ was synthesized via one-pot hydrothermal synthesis to form a Z-scheme heterojunction, showing enhanced photocatalytic activity compared with the pure substance [20]. Xu et al. successfully synthesized the Bi_2S_3-sensitized $Bi_2Sn_2O_7$ (BSO) photocatalyst (Bi_2S_3/BSO) via a simple and economical thioacetamide (CH_3CSNH_2) ion exchange method [21]. Under visible light irradiation ($\lambda > 420$ nm), the Bi_2S_3/BSO heterojunction exhibits excellent photocatalytic performance in the decomposition of Rhodamine B (RhB). However, there has been limited research on the use of $Bi_2Sn_2O_7$ for indoor air pollution control, particularly in reducing gaseous NO_x.

Recently, the surface plasmon resonance (SPR) effect of noble metals such as gold and silver has been used to enhance the visible light catalytic activity of semiconductor photocatalysts [22,23]. The collective oscillation of free electrons in noble metals gives rise to the SPR effect, resulting in strong absorption in the solar region. Low-cost bismuth metal also exhibits the SPR effect, and can be applied as a plasmonic co-catalyst to enhance the photocatalytic activity of other semiconductors due to its significant advantages. For example, Bi/Bi_2MoO_6 [24], Bi/g-C_3N_4 [25], Bi/TiO_2 [26], and Bi/BiOCl [27] showed a higher photocatalytic performance after loading metallic Bi, because the SPR effect enhances photoabsorption ability and promotes charge separation.

In this study, the SPR effect was used to cause the excitation of photogenerated e^--h^+ pairs in $Bi_2Sn_2O_7$ by depositing Bi nanodots on the surface of sheet-like $Bi_2Sn_2O_7$. The photocatalytic activity of flaky $Bi_2Sn_2O_7$ was evaluated by oxidizing NO at a ppb level under xenon lamp ($\lambda > 400$ nm) irradiation [28]. The effect of Bi loading on the performance of $Bi_2Sn_2O_7$ was systematically studied, and the present study supports the use of Bi in $Bi_2Sn_2O_7$ to enhance the photocatalytic performance of composite photocatalysts. Its reaction mechanism was also investigated.

2. Results and Discussion

2.1. Phase Analysis

The phase and crystal structure of the samples were tested by XRD, as shown in Figure 1. For the pristine $Bi_2Sn_2O_7$ (BSO), there are four peaks at 28.8°, 33.4°, 47.9° and

56.9°, which can be indexed to (222), (400), (440), and (622) of cubic $Bi_2Sn_2O_7$ (JCPDS No. 87-0284), indicating that the prepared $Bi_2Sn_2O_7$ was successfully synthesized and has a good crystallinity. Then, Bi was deposited in situ from BSO by adding a concentration of $NaBH_4$. A series of $Bi/Bi_2Sn_2O_7$ (B-BSO-x, x represents the concentration of $NaBH_4$) was obtained. However, compared with pure $Bi_2Sn_2O_7$, the composites have no new additional peaks and no peaks belonging to Bi^0, possibly due to the low content of Bi^0.

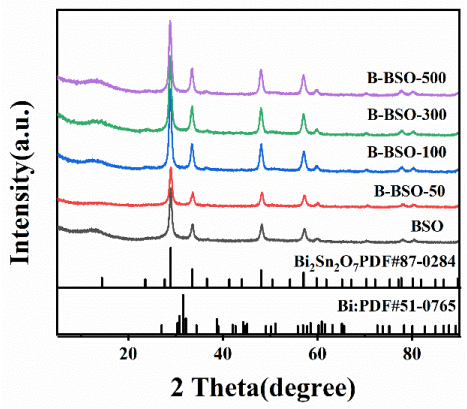

Figure 1. XRD pattern of B/BSO nanoparticles.

2.2. Morphology

Figure 2 shows the TEM images used to characterize the morphologies and analyze element composition of pure $Bi_2Sn_2O_7$ and $Bi/Bi_2Sn_2O_7$ composites. Figure 2a shows that pure $Bi_2Sn_2O_7$ comprises uniform nanosheets with an average dimension of 5–10 nm. After loading Bi, the composite (B-BSO-300) still maintains the same morphology, as shown in Figure 2c, implying that metal Bi is reduced from BSO and deposited on BSO. In Figure 2b,d, high-resolution TEM (HRTEM) images of $Bi_2Sn_2O_7$ and B-BSO-300 are shown. The lattice distance of pure $Bi_2Sn_2O_7$ is 0.2678 nm, corresponding to the (400) plane (Figure 2b). Additionally, B-BSO-300 (Figure 2d) has two lattice fringes of 0.1884 nm and 0.28 nm, which are indexed as the (440) lattice plane of $Bi_2Sn_2O_7$ and the (012) lattice plane of Bi. Additionally, the EDS elemental mappings of B-BSO-300 contain Bi, O, and Sn elements. Thus, the TEM analysis demonstrates the successful preparation of $Bi/Bi_2Sn_2O_7$.

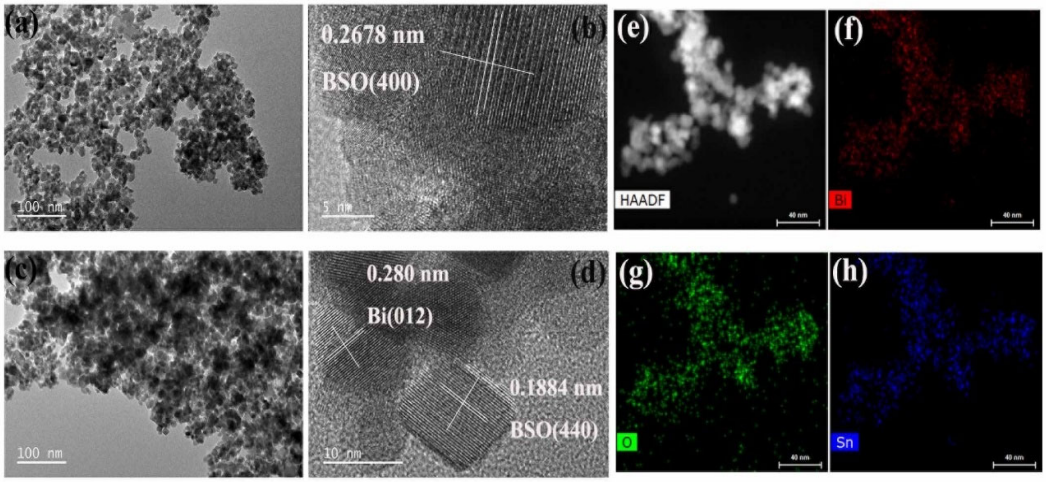

Figure 2. (**a**,**c**) TEM image of BSO and B-BSO-300; (**b**) HRTEM image of BSO; (**d**) HRTEM image of B-BSO-300; (**e**) HAADF-STEM image of B-BSO-300; (**f**–**h**) EDS elemental mappings of (**f**) Bi, (**g**) O, (**h**) and Sn from panel (**e**).

2.3. Chemical Compositions

X-ray photoelectron spectroscopy (XPS) was conducted to study the chemical composition and element states of BSO, B-BSO-300, and B-BSO-300 (30 s). As shown in Figure 3a–c, the XPS survey spectra of the samples reveals the existence of Bi, Sn, O and C. For BSO, the Bi 4f can be fitted to 164.87 and 159.57 eV, which are attributed to Bi $4f_{7/2}$ and Bi $4f_{5/2}$ of Bi^{3+}, respectively. However, B-BSO-300 with deposited Bi only has Bi^{3+} peaks and no new peaks of Bi^0, which is possibly due to the easy oxidation of surficial Bi^0 [29]. After Ar etching for 30 s, B-BSO-300 (30 s) has two new peaks at 156.7 eV and 162.3 eV, belonging to metal Bi, which is in agreement with a previous study [30]. The existence of metal Bi directly verifies the successful loading of Bi. The Sn 3d of these three samples consists of two character peaks located at 486.42 eV (attributed to Sn^{4+} $3d_{5/2}$) and 495.42 eV(Sn^{4+} $3d_{3/2}$) in Figure 3e. Figure 3f shows the XPS spectra of O1s. BSO and B-BSO-300 have only one peak assigned to O1s of O^{2-} [13]. B-BSO-300 (30 s) has new peaks at 532–534 eV, which are possibly caused by oxygen vacancies [31].

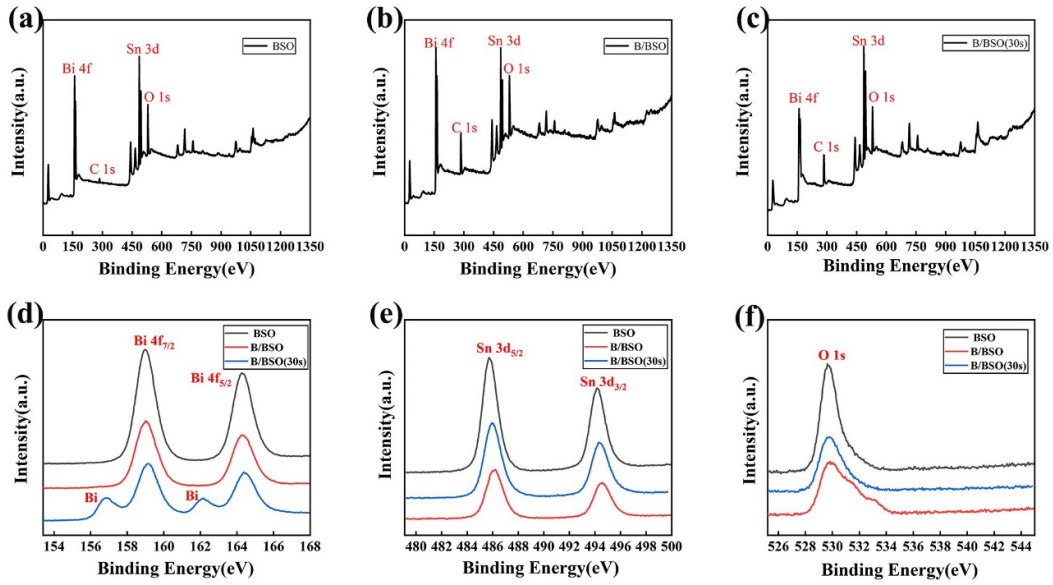

Figure 3. The wide-scan XPS spectra of (**a**) BSO, (**b**) B-BSO-300, and (**c**) B-BSO-300 (30 s); high-resolution XPS spectra of (**d**) Bi 4f, (**e**) Sn 3d, and (**f**) O 1s.

2.4. Photocatalytic Performance

Photocatalytic NO removal is always a complicated process, yielding a final product of HNO_3 and the toxic intermediate NO_2. Firstly, 0.05 g photocatalysts were deposited on a glass surface (10 × 5 cm) to test photocatalytic NO removal performance in an atmosphere of NO with a concentration of about 500 ppb. Under visible light irradiation, the efficiency of NO removal and the production of the toxic intermediate NO_2 over $Bi_2Sn_2O_7$ and $Bi/Bi_2Sn_2O_7$ composites were evaluated to judge photocatalytic performance. As shown in Figure 4a, pure BSO reaches an equilibrium within 10 min and has a NO removal rate at 7.2%. After the surface modification of Bi, the photocatalytic activities of the composites all significantly increased. The photocatalytic NO removal efficiencies of B-BSO-50, B-BSO-100, B-BSO-300, and B-BSO-500 are about 8.1%, 21.8%, 38.6% and 27.8%, respectively, indicating that B-BSO-300 has the best photocatalytic performance with the optimal content of metal Bi. The excessive loading of Bi has a negative effect on photocatalytic NO conversion, probably due to the cover of the surficial active sites of BSO and the excess break of BSO photocatalysts [32–34].

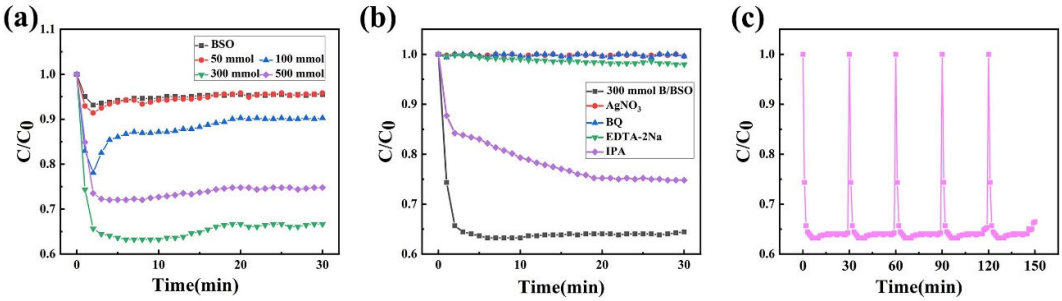

Figure 4. NO removal by pure BSO and B-BSO in different proportions under visible light: (**a**) C/C_0, (**b**) effect of different capture agents on NO removal using B-BSO-300 photocatalyst, and (**c**) cycle experiment of NO removal using B-BSO-300 photocatalyst under visible light irradiation.

The active species is an important factor for exploring the photocatalytic reaction process and its efficiency. In order to inspect the main active species in the photodegradation process, benzoquinone (BQ), ethylenediaminetetraacetic acid disodium (EDTA-2Na), $AgNO_3$, and isopropanol (IPA) were selected as the scavengers of $\bullet O_2^-$, h^+, e^-, and •OH for the trapping experiment, using B-BSO-300 as a photocatalyst [35]. As shown in Figure 4b, in the presence of BQ, EDTA-2Na, and $AgNO_3$, the photocatalytic NO removal efficiency of B-BSO-300 was mostly reduced, confirming that $\bullet O_2^-$, h^+, e^- radicals were the first active species to cause NO oxidation. However, the photocatalytic efficiency of NO was partly inhibited after the addition of IPA, suggesting that •OH is the second active species. The scavenger tests demonstrate that the photocatalytic removal of NO is a result of interactions between active species.

The photocatalytic stability of these photocatalysts restricts their practical application. Figure 4c shows the stability of B-BSO-300. In the process of five cycles, B-BSO-300 showed no decrease in the NO removal rate, indicating the composite has an excellent photocatalytic durability. Furthermore, the generation of toxic intermediate NO_2 is effectively hindered, as shown in Figure 5. It is clear that the NO_2 production of the samples gradually decreases as the Bi content increases, until B-BSO-300 exhibits the lowest NO_2 generation, indicating that all produced NO_2 is further oxidized to nitrates. This indicates that the Bi modification can effectively improve NO selectivity to the final products: nitrates rather than the toxic NO_2.

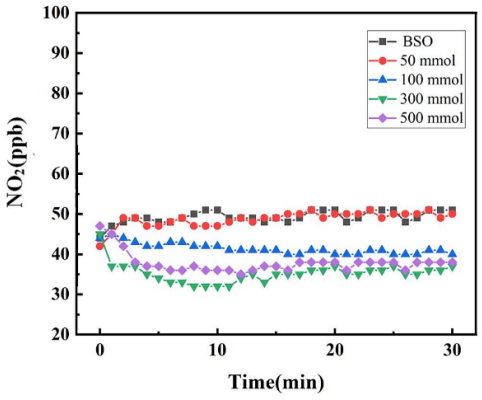

Figure 5. C/C_0 of NO_2 when NO is removed by visible light with pure BSO and B-BSO in different proportions.

2.5. Charge Generation and Transfer

The excellent separation efficiency of the carrier charge can give materials a good photocatalytic activity. Photoluminescence (PL) emissions were utilized to analyze the separation efficiency of photogenerated electrons and holes. Commonly, the PL intensity is proportional to the recombination rate of photogenerated carriers. The PL spectra of BSO and B-BSO-300 at a 365 nm excitation is shown in Figure 6. Evidently, the peak intensity

of B-BSO-300 is lower than that of BSO, which indicates that the reduced Bi nanodots inhibit the carriers' recombination and improve the separation efficiency of photogenerated carriers, which can significantly optimize photocatalytic performance.

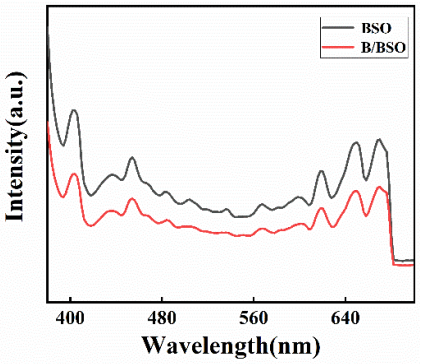

Figure 6. PL spectra of pure BSO and B-BSO-300 in different proportions.

Electrochemical tests were conducted to further elucidate the separation and migration of photogenerated carriers. The higher transient photocurrent performs a higher concentration and separation of carriers. As shown in Figure 7a, the transient photocurrent response spectra show that pristine BSO has a poor photocurrent, indicating a low photoelectric conversion efficiency. After reducing Bi, B-BSO exhibits a stronger current response than BSO, and B-BSO-300 has the best response, which proves that the introduction of Bi can effectively promote the separation of photogenerated carriers. Similarly, the electrochemical impedance spectroscopy (EIS) in Figure 7b shows that the interfacial charge transfer resistance of B-BSO is relatively weaker than BSO, which is beneficial for transporting photogenerated carriers. A proper band structure is very important for the photocatalytic oxidation/reduction ability of photocatalysts. The Mott–Schottky (MS) spectrum is shown in Figure 7c. The positive slope shows that BSO is a typical n-type semiconductor and its flat-band potential (V_{fb}) is −0.38 V [36]. In general, the conductive level of the n-type semiconductor is close to the flat-band potential [37,38]. The conduction band of BSO is −0. 38 eV Ag/AgCl relative to PH 6.8 (equivalent to −0. 28 NHE relative to PH 6.8) [39].

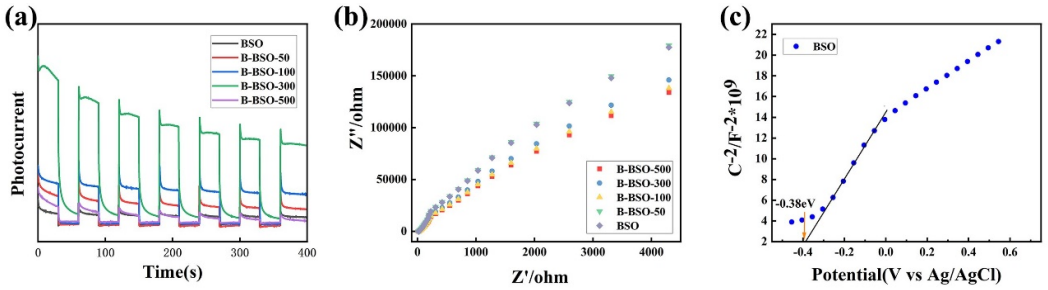

Figure 7. (**a**) Transient photocurrent of BSO and B-BSO series, (**b**) EIS of BSO and B-BSO series, and (**c**) MS spectrum of pure BSO.

The photoresponse efficiency is another factor of photocatalytic efficiency. UV–vis diffuse reflectance spectra (DRS) can be used to effectively characterize the optical properties of the samples, and the bandgap is calculated by analyzing these spectra. As displayed in Figure 8a, all samples showed absorption bands in the visible region. Pure BSO has a relatively weak absorption in visible region and has an absorption edge at about 520 nm. After the deposition of Bi nanoparticles, B-BSO displays a slight red-shift of the absorption edge and enhanced light absorption in the visible region, which can be attributed to the SPR effect of Bi [40]. The absorption peak in the range of 500–700 nm is potentially the SPR absorption peak. As the Bi content increases in BSO, the SPR absorption intensity rises, and B-BSO-300 has the best absorption in the range of 300–800 nm. It is worth noting that the

slope of the band edge decreases gradually after the introduction of Bi nanodots, indicating that the band gap of the composites becomes smaller, which proves that the intrinsic absorption capacity of B-BSO is also enhanced. The band gap(Eg) of BSO is calculated using the Kubelka–Munk function [41]. As shown in Figure 8b, the Eg of BSO is 2.42 eV. According to Eg = $E_{CB} - E_{VB}$, E_{VB} is calculated as 2.14 eV [42].

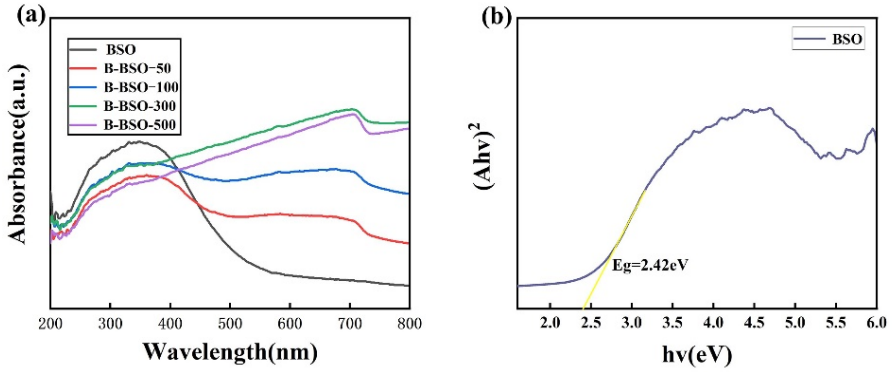

Figure 8. (**a**) DRS of pure BSO and B-BSO with different proportions; (**b**) the corresponding Tauc plots of BSO.

2.6. The Role of Bi in the Enhanced Production of Reactive Species

To investigate the main active radical species on B-BSO nanoplates for the NO removal, TEMPO and DMPO spin-trapping ESR analyses over pure BSO and B-BSO-300 for TEMPO-e^-, DMPO-h^+, DMPO-$\bullet O_2^-$ and DMPO-•OH were performed, and the results are shown in Figure 9. The TEMPO signal is found under dark conditions, and the peak gradually becomes smaller as the exposure time to visible light increases, demonstrating that a lot of electrons are generated and consumed by the conversion from TEMPO to TEMPOH. Compared with BSO (Figure 9a) and B-BSO-300 (Figure 9b), the composite can produce many more electrons than single BSO. Meanwhile, Figure 9c,d show that the composite can produce more h^+ under irradiation than BSO. Furthermore, as shown in Figure 9e–h, the characteristic peaks of $\bullet O_2^-$ and •OH were not detected in the dark. However, under light irradiation, the $\bullet O_2^-$ and •OH radicals can be detected. Additionally, compared with BSO, the composites have much stronger $\bullet O_2^-$ and •OH radicals, suggesting that loading Bi can help BSO generate more $\bullet O_2^-$ and •OH radicals for stronger oxidization reactions.

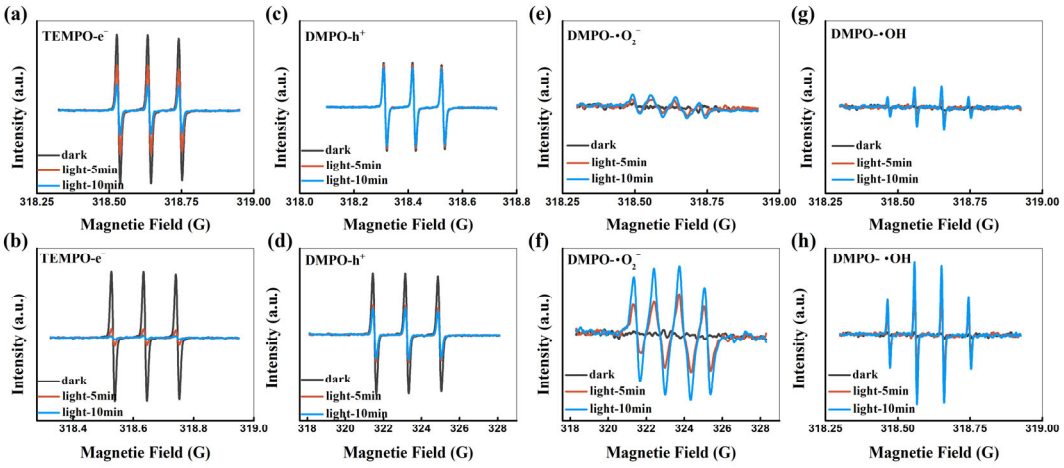

Figure 9. ESR spectra of (**a**) e^-, (**c**) h^+, and (**e**) $\bullet O_2^-$; (**g**) •OH of BSO and (**b**) e^-, (**d**) h^+, (**f**) $\bullet O_2^-$, (**h**) •OH of B-BSO-300 at room temperature.

2.7. Analysis of the Photocatalytic Mechanism

According to literature reports, photocatalytic reactions involve three main reaction steps [43]: (1) Photoexcitation step: photocatalytic semiconductor materials absorb photons to generate electron–hole pairs, which have redox capability in the conduction and valence band. (2) Separation and migration of charge carriers: electrons and holes are transferred to the surface to hinder the recombination of carriers under Coulomb forces. (3) The catalytic reaction process at the surface of the material: electrons and holes quickly react with the surficial O_2 and absorbed H_2O to produce active species, highly active $\bullet O_2^-$ and •OH, which undergo oxidation–reduction reactions.

Based on the above analysis, a possible photocatalytic mechanism was proposed as shown in Figure 10. The conduction band potential (E_{CB}) of BSO was −0.28 eV and the valence band potential (E_{VB}) of BSO was 2.14 eV, based on DRS and MS analysis. E_{CB} of BSO (−0.28 eV) has a more negative reduction potential than that of $O_2/\bullet O_2^-$ (−0.046 eV vs. NHE), suggesting that the photoexcited electrons in the conduction band can reduce O_2 to $\bullet O_2^-$ [44]. Meanwhile, the E_{VB} of BSO is 2.14 eV, meaning that BSO has more oxidation potential than $OH^-/\bullet OH$ (1.99 eV vs. NHE) [45]. The photogenerated h^+ will oxidize H_2O into •OH radicals, consistent with the ESR results (Figure 9). These analyses show that the formation of $\bullet O_2^-$ and •OH radicals in the photocatalytic process is thermodynamically advantageous in the prepared BSO samples.

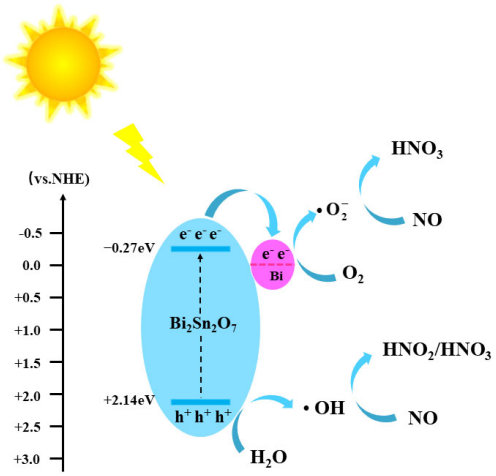

Figure 10. Photocatalytic mechanism diagram.

For the Bi/BSO composites, the Fermi level (vs. NHE) of Bi is reported to be −0.17 eV, which is more positive than E_{CB} of BSO, demonstrating that Bi can capture electrons from BSO [46]. Therefore, under light irradiation, the photogenerated electrons of BSO are transferred to Bi and then react O_2 to $\bullet O_2^-$, while the photoinduced holes of BSO oxidize H_2O into •OH radicals. Then, the •OH oxidizes NO pollutants directly to HNO_2 and HNO_3 due to its reactive effect [47]. Furthermore, the $\bullet O_2^-$ can oxidize NO to NO_3 [48], and the loading Bi can cause an increase in NO removal and decrease in NO_2 production, mainly ascribed to the high production of $\bullet O_2^-$ and •OH [49]. Strong oxidation radicals can help improve oxidation to produce HNO_3. Finally, the introduction of Bi not only enhances the SPR-induced photoresponse ability, but also improves the separation of photogenerated carriers and the oxidation ability of the radicals to produce HNO_3 [50].

3. Experimental Section

3.1. Materials and Reagents

All chemicals used were analytically pure and could be used directly without further purification. $Bi(NO_3)_3{\cdot}5H_2O$, $Na_2SnO_3{\cdot}4H_2O$ and NaOH were purchased from Shanghai Macklin Biotechnology Co., Ltd. (Shanghai, China). PVP and $NaBH_4$ were purchased from Shanghai Aladdin Biochemical Technology Co., Ltd. (Shanghai, China).

3.2. Preparation of Photocatalysts

A one-step hydrothermal method was used to synthesize $Bi_2Sn_2O_7$. Firstly, 3 mmol of $Na_2SnO_3{\cdot}4H_2O$ and 3 mmol of $Bi(NO_3)_3{\cdot}5H_2O$ were dispersed into 80 mL of deionized water. After that, the pH value of the obtained mixture was adjusted to 12 with the NaOH solution (3 M). The mixture was subsequently transferred into a 100 mL Teflon-lined autoclave to undergo a hydrothermal process at 180 °C for 12 h. Finally, the precipitate was washed thoroughly with deionized water and dried in a vacuum oven at 60 °C for 12 h.

BSO was prepared with in situ deposited Bi nanodots in a simple reduction reaction. Next, 2 mmol of BSO was dispersed into 100 mL of deionized water containing 1.0 g of PVP (polyvinylpyrrolidone) and stirred for 20 min. A specific concentration of $NaBH_4$ (30 mL) was then added dropwise to the suspension. Next, the resulting suspension was stirred for 1 h, and the precipitates were collected by centrifugation, washed four times with ethanol and deionized water, and air-dried at 60 °C. The concentrations of $NaBH_4$ were 50, 100, 300, and 500 mmol/L; the resulting samples were marked as B-BSO-50, B-BSO-100, B-BSO-300, and B-BSO-500, respectively.

3.3. Catalyst Characterization

The phase characters were tested through a Bruker D8 Advance X-ray diffractometer (XRD) using CuK radiation with 5–80° (Bruker, Billerica, MA, USA). The morphology of the samples was detected by transmission electron microscopy (TEM) and high-resolution transmission electron microscopy (HRTEM), using the FEI Tecnai G2 F20 (FEI, Hillsboro, OR, USA). The elemental distribution scanning (EDS) elemental mappings were detected by Tecnai G2 F30 with Esax Genesis (FEI, Hillsboro, OR, USA). The chemical compositions and element valence state were analyzed by X-ray photoelectron spectroscopy (XPS) using Thermo ESCALAB 250× (Thermo Fisher Scientific, Waltham, MA, USA). The photoluminescence (PL) spectrum was tested under the excitation wavelength of 365 nm using the FLS980 spectrometer (Edinburgh Instruments, Livingston, Scotland). The electrochemical tests were measured on a CHI760e electrochemical working station in a pH = 7, 0.5 M sodium sulfate solution electrolyte. The ultraviolet–visible diffuse reflectance spectra (DRS) were measured with a Hitachi UV-4100 spectrophotometer using $BaSO_4$ as the reflectance standard (Hitachi, Tokyo, Japan). The electron spin resonance (ESR) signals were obtained on a Bruker-type ESR JES-FA200 spectrometer equipped with a quantum ray Nd, utilizing YAG laser as a light source and a UV cut-off filter ($\geq$400 nm) (Bruker, Billerica, MA, USA).

3.4. Photocatalytic NO Removal Performance Test

The photocatalytic activity of the system was evaluated by oxidizing NO at room temperature using the Beijing Perfect Light PLR-GSPR atmospheric-pressure gas–solid photocatalytic reaction system (Beijing Perfect Light Technology Co., Ltd., Beijing, China). The visible light source used was from a 300WXe lamp (PLS-SXE300D, Beijing Perfect Light Technology Co., Ltd., Beijing, China) with a cut-off filter ($\lambda > 400$ nm). The reactor was a square stainless steel vessel with a quartz top window, and the distance from the xenon lamp to the quartz top window was set at 20 cm. Photocatalyst powder (0.05 g) was deposited on a glass surface (10 × 5 cm). NO gas was supplied from a compressed gas cylinder with 50 ppm NO (diluted with O_2), diluting the initial NO concentration to about 500 ppb. The flow rates of gas flow and NO were controlled at 2.4 $Lmin^{-1}$ and 15 $mLmin^{-1}$, respectively. The two streams are then premixed in a three-way valve. The relative humidity in the airflow was controlled at 50%. When adsorption–desorption equilibrium is reached, the lamp is turned on. NO was measured every 1 min using a NO_x concentration analyzer (Thermo Scientific, 42i-TL, Waltham, MA, USA), which also monitors the concentrations of NO_2 and NO_x (NO_x stands for NO + NO_2). The calculation formula of NO removal rate (η) is η (%) = $(1 - C/C_0) \times 100\%$, where C is the outlet concentration of NO after the reaction time t, and C_0 is the inlet concentration after reaching the adsorption–desorption equilibrium.

3.5. Scavenging Experiments of Active Species

Active species trapping experiments were used to elucidate the role of different radicals and charge carriers in the photocatalytic removal of NO at an ambient temperature. The scavenging agents, benzoquinone (BQ), disodium ethylenediaminetetraacetate (Na_2-EDTA), $AgNO_3$, and isopropanol (IPA), were added to the system containing the BSO and B-BSO-300 samples. In the photocatalytic reaction process, they capture photo-generated superoxide ($\bullet O^{2-}$), holes (h^+), electrons (e^-), and hydroxyl ($\bullet$OH) radicals, respectively. The reaction is monitored within the same irradiation time as the control experiment to compare removal efficiency.

4. Conclusions

In summary, a novel Bi-$Bi_2Sn_2O_7$ nanohybrid photocatalyst with a high photocatalytic ability was constructed. Compared with BSO alone, the B-BSO nanocomposite exhibits effective visible-light photocatalytic performance for NO removal. Due to the SPR effect of Bi metal, the significant increase in light absorption and the improvement of charge separation efficiency contributed to enhanced photocatalytic activity. The photocatalytic NO removal rate of B/BSO increased from 7.2% to 38.6%. This SPR effect not only promotes the transfer of photogenerated electrons, but also promotes the separation and migration of photogenerated carriers, enhancing the generation of $\bullet O_2^-$ and $\bullet$OH radicals responsible for the oxidation of NO. The B-BSO composite photocatalyst also exhibits excellent photocatalytic stability, making it a potential candidate for use in air purification systems. This study not only provides new insights into the synthesis of bismuth-based metal semiconductor nanocomposite photocatalysts, but also demonstrates the feasibility of using cheap and abundant bismuth metal for cocatalysts to improve photocatalytic efficiency.

Author Contributions: Conceptualization, N.L.; validation, L.G.; formal analysis, W.Z.; investigation, W.Z. and X.L.; Resource, L.G.; data curation, J.Z., X.L. and Y.G.; writing—original draft preparation, W.Z., J.Z. and X.L.; writing—review and editing, N.L.; Visualization, Y.G.; supervision, L.G.; project administration, L.G.; funding acquisition, N.L. All authors have read and agreed to the published version of the manuscript.

Funding: This study was financially supported by National Natural Science Foundation of China (NSFC 51802351) and Tianjin Key Laboratory of Building Green Functional Materials (2024LSJZCL-05).

Data Availability Statement: The data presented in this study are available on request.

Conflicts of Interest: The authors declare no competing financial interests.

References

1. Chi, X.; Mandal, L.; Liu, C.; Fauzi, A.D.; Chaudhuri, A.; Whitcher, T.J.; Jani, H.K.; Chen, Z.; Xi, S.; Diao, C.; et al. Unravelling a new many-body large-hole polaron in a transition metal oxide that promotes high photocatalytic activity. *NPG Asia Mater.* **2022**, *14*, 61–67. [CrossRef]
2. Li, F.; Liu, G.; Liu, F.; Yang, S. A review of self-cleaning photocatalytic surface: Effect of surface characteristics on photocatalytic activity for NO. *Environ. Pollut.* **2023**, *327*, 121580. [CrossRef] [PubMed]
3. Oluwole, A.O.; Olatunji, O.S. Photocatalytic degradation of tetracycline in aqueous systems under visible light irridiation using needle-like SnO_2 nanoparticles anchored on exfoliated g-C_3N_4. *Environ. Sci. Eur.* **2022**, *34*, 931–943. [CrossRef]
4. Cao, C.; Xing, L.; Yang, Y.; Tian, Y.; Ding, T.; Zhang, J.; Hu, T.; Zheng, L.; Li, X. The monolithic transition metal oxide crossed nanosheets used for diesel soot combustion under gravitational contact mode. *Appl. Surf. Sci.* **2017**, *406*, 245–253. [CrossRef]
5. Wu, H.; Chen, R.; Wang, H.; Cui, W.; Li, J.; Wang, J.; Yuan, C.; Zhuo, L.; Zhang, Y.; Dong, F. An atomic insight into BiOBr/$La_2Ti_2O_7$ p-n heterojunctions: Interfacial charge transfer pathway and photocatalysis mechanism. *Catal. Sci. Technol.* **2020**, *10*, 826–834. [CrossRef]
6. Zhu, P.; Yin, X.; Gao, X.; Dong, G.; Xu, J.; Wang, C. Enhanced photocatalytic NO removal and toxic NO_2 production inhibition over ZIF-8-derived ZnO nanoparticles with controllable amount of oxygen vacancies. *Chin. J. Catal.* **2021**, *42*, 175–183. [CrossRef]
7. Hou, J.; Cao, S.; Wu, Y.; Liang, F.; Sun, Y.; Lin, Z.; Sun, L. Simultaneously efficient light absorption and charge transport of phosphate and oxygen-vacancy confined in bismuth tungstate atomic layers triggering robust solar CO_2 reduction. *Nano Energy* **2017**, *32*, 359–366. [CrossRef]
8. Zha, R.; Niu, Y.; Liu, C.; He, L.; Zhang, M. Oxygen vacancy configuration in confined $BiVO_4$-Bi_2S_3 heterostructures promotes photocatalytic oxidation of NO. *J. Environ. Chem. Eng.* **2021**, *9*, 106586. [CrossRef]

9. Li, G.; Lian, Z.; Wan, Z.; Liu, Z.; Qian, J.; Deng, Y.; Zhang, S.; Zhong, Q. Efficient photothermal-assisted photocatalytic NO removal on molecular cobalt phthalocyanine/Bi_2WO_6 Z-scheme heterojunctions by promoting charge transfer and oxygen activation. *Appl. Catal. B-Environ.* **2022**, *317*, 121787. [CrossRef]
10. Xie, W.; Wang, Y.; Du, R.; Hu, X.; Wang, H.; Huang, J.; Xiang, Y.; Song, H.; Cai, Y.; Li, Z.; et al. Insights into the atomic structure of oxygen vacancy on Bi_2MoO_6/MXene heterojunction and its role for boosting photocatalytic NO oxidation. *Appl. Surf. Sci.* **2023**, *638*, 158104. [CrossRef]
11. Wang, Z.; Huang, Y.; Ho, W.; Cao, J.; Shen, Z.; Lee, S.C. Fabrication of $Bi_2O_2CO_3$/g-C_3N_4 heterojunctions for efficiently photocatalytic NO in air removal: In-situ self-sacrificial synthesis, characterizations and mechanistic study. *Appl. Catal. B-Environ.* **2016**, *199*, 123–133. [CrossRef]
12. Liao, J.; Li, K.; Ma, H.; Dong, F.; Zeng, X.; Sun, Y. Oxygen vacancies on the BiOCl surface promoted photocatalytic complete NO oxidation via superoxide radicals. *Chin. Chem. Lett.* **2020**, *31*, 2737–2741. [CrossRef]
13. Zhao, X.; Yu, J.; Cui, H.; Wang, T. Preparation of direct Z-scheme $Bi_2Sn_2O_7$/g-C_3N_4 composite with enhanced photocatalytic performance. *J. Photochem. Photobiol. A-Chem.* **2017**, *335*, 130–139. [CrossRef]
14. Liu, Y.; Gong, Y.; Cui, X.; Lu, Y.; Yu, H.; Qin, W.; Huo, M. Visible-light activation of persulfate by a Z-scheme photocatalyst Fe-C_3N_4/$Bi_2Sn_2O_7$ for tetracycline degradation. *Appl. Catal. A-Gen.* **2023**, *666*, 119422. [CrossRef]
15. Fu, Q.; He, T.; Li, J.L.; Yang, G.W. Surface effect on electronic and optical properties of $Bi_2Ti_2O_7$ nanowires for visible light photocatalysis. *J. Appl. Phys.* **2012**, *111*, 449–471. [CrossRef]
16. Ren, J.; Liu, G.; Wang, Y.; Shi, Q. A novel method for the preparation of $Bi_2Ti_2O_7$ pyrochlore. *Mater. Lett.* **2012**, *76*, 184–186. [CrossRef]
17. Wang, T.; Liu, X.; Men, Q.; Ma, W.; Liu, Z.; Liu, Y.; Ma, C.; Huo, P.; Yan, Y. Photocatalytic removal using g-C_3N_4 quantum dots/$Bi_2Ti_2O_7$ composites. *Spectrochim. Acta Part A-Mol. Biomol. Spectrosc.* **2019**, *213*, 19–27. [CrossRef] [PubMed]
18. Li, Y.-J.; Cao, T.-P.; Zhao, Y.-H.; Sun, D.-W.; Wang, X. Preparation of Bi@$Bi_2Sn_2O_7$/TiO_2 Plasmonic Composite Fibers with Enhanced Photocatalytic Hydrogen Generation Activity. *Chin. J. Inorg. Chem.* **2019**, *35*, 1371–1378.
19. Zhang, Y.; Di, J.; Qian, X.; Ji, M.; Tian, Z.; Ye, L.; Zhao, J.; Yin, S.; Li, H.; Xia, J. Oxygen vacancies in $Bi_2Sn_2O_7$ quantum dots to trigger efficient photocatalytic nitrogen reduction. *Appl. Catal. B-Environ.* **2021**, *299*, 931–943. [CrossRef]
20. Huang, S.; Zhang, J.; Qin, Y.; Song, F.; Du, C.; Su, Y. Direct Z-scheme SnO_2/$Bi_2Sn_2O_7$ photocatalyst for antibiotics removal: Insight on the enhanced photocatalytic performance and promoted charge separation mechanism. *J. Photochem. Photobiol. A-Chem.* **2021**, *404*, 449–471. [CrossRef]
21. Xu, W.; Fang, J.; Chen, Y.; Lu, S.; Zhou, G.; Zhu, X.; Fang, Z. Novel heterostructured Bi_2S_3/$Bi_2Sn_2O_7$ with highly visible light photocatalytic activity for the removal of rhodamine B. *Mater. Chem. Phys.* **2015**, *154*, 30–37. [CrossRef]
22. Dejpasand, M.T.; Saievar-Iranizad, E.; Bayat, A.; Ardekani, S.R. Surface plasmon-induced photodegradation of methylene blue with single layer graphene quantum dots/Au nanospheres under visible-light irradiation. *J. Alloys Compd.* **2021**, *885*, 931–943. [CrossRef]
23. Rawool, S.A.; Pai, M.R.; Banerjee, A.M.; Nath, S.; Bapat, R.D.; Sharma, R.K.; Jagannath, B.; Dutta, B.; Hassan, P.A.; Tripathi, A.K. Superior Interfacial Contact Yields Efficient Electron Transfer Rate and Enhanced Solar Photocatalytic Hydrogen Generation in M/C_3N_4 Schottky Junctions. *ACS Appl. Mater. Interfaces* **2023**, *15*, 39926–39945. [CrossRef] [PubMed]
24. Li, J.; Wang, B.; Pang, Y.; Sun, M.; Liu, S.; Fang, W.; Chen, L. Fabrication of 0D/1D Bi_2MoO_6/Bi/TiO_2 heterojunction with effective interfaces for boosted visible-light photocatalytic degradation of tetracycline. *Colloids Surf. A-Physicochem. Eng. Asp.* **2022**, *638*, 449–471. [CrossRef]
25. Karimi-Nazarabad, M.; Goharshadi, E.K. Decoration of graphene oxide as a cocatalyst on Bi doped g-C_3N_4 photoanode for efficient solar water splitting. *J. Electroanal. Chem.* **2022**, *904*, 13576–13582. [CrossRef]
26. Sun, Y.; Feng, B.; Li, Q.; Tian, C.; Ma, L.; Li, Z. The Application of Bi-Doped TiO_2 for the Photocatalytic Oxidation of Formaldehyde. *Cryst. Res. Technol.* **2022**, *57*, 931–943. [CrossRef]
27. Wang, L.; Wang, R.; Qiu, T.; Yang, L.; Han, Q.; Shen, Q.; Zhou, X.; Zhou, Y.; Zou, Z. Bismuth Vacancy-Induced Efficient CO_2 Photoreduction in BiOCl Directly from Natural Air: A Progressive Step toward Photosynthesis in Nature. *Nano Lett.* **2021**, *21*, 10260–10266. [CrossRef]
28. Zhang, L.; Yang, C.; Lv, K.; Lu, Y.; Li, Q.; Wu, X.; Li, Y.; Li, X.; Fan, J.; Li, M. SPR effect of bismuth enhanced visible photoreactivity of Bi_2WO_6 for NO abatement. *Chin. J. Catal.* **2019**, *40*, 755–764. [CrossRef]
29. Xin, Y.; Zhu, Q.; Gao, T.; Li, X.; Zhang, W.; Wang, H.; Ji, D.; Huang, Y.; Padervand, M.; Yu, F.; et al. Photocatalytic NO removal over defective Bi/BiOBr nanoflowers: The inhibition of toxic NO_2 intermediate via high humidity. *Appl. Catal. B-Environ.* **2023**, *324*, 122238. [CrossRef]
30. Li, H.; Li, H.; Zhou, Z.; Tong, H.; Long, B.; Liu, W.; Li, W. Tailoring hydrophily and composition of BiOI for an ultrafast photodegradation of tetracycline hydrochloride. *J. Environ. Chem. Eng.* **2021**, *9*, 13576–13582. [CrossRef]
31. Guo, S.; Di, J.; Chen, C.; Zhu, C.; Duan, M.; Lian, C.; Ji, M.; Zhou, W.; Xu, M.; Song, P.; et al. Oxygen vacancy mediated bismuth stannate ultra-small nanoparticle towards photocatalytic CO_2-to-CO conversion. *Appl. Catal. B-Environ.* **2020**, *276*, 119156. [CrossRef]
32. Liu, T.; Cheng, Z.; Shi, T.; Yang, S.; Zhang, Y. Atomically thin Bi/$Bi_4Ti_3O_{12}$ heterojunction mediated increasing active photogenerated carriers for boosting photocatalytic activity. *J. Colloid Interface Sci.* **2022**, *613*, 625–635. [CrossRef]

33. Puga, F.; Navio, J.A.; Cordoba, J.M.; Romero-Sarria, F.; Hidalgo, M.C. Insights into the structural and physicochemical properties of Zn-Bi-O composites for efficient photodegradation of caffeic acid, rhodamine B and methyl orange. *Appl. Surf. Sci.* **2022**, *581*, 931–943. [CrossRef]
34. Yang, Y.; Bian, Z.; Zhang, L.; Wang, H. Bi@$BiO_x(OH)_y$ modified oxidized g-C_3N_4 photocatalytic removal of tetracycline hydrochloride with highly effective oxygen activation. *J. Hazard. Mater.* **2022**, *427*, 931–943. [CrossRef]
35. Fenelon, E.; You, S.-J.; Wang, Y.-F. Photodegradation of Nitrogen Oxide under Solar Light Using a Facile Synthesis Catalyst. *Aerosol Air Qual. Res.* **2021**, *21*, 931–943. [CrossRef]
36. Chen, L.; Li, C.; Zhao, Y.; Wu, J.; Li, X.; Qiao, Z.; He, P.; Qi, X.; Liu, Z.; Wei, G. Constructing 3D Bi/$Bi_4O_5I_2$ microspheres with rich oxygen vacancies by one-pot solvothermal method for enhancing photocatalytic activity on mercury removal. *Chem. Eng. J.* **2021**, *425*, 449–471. [CrossRef]
37. Liu, X.; Zhang, Y.; Wang, H.; Yan, J.; Yan, L.; Li, K.; Guo, H.; Gong, W.; Lin, J. Highly efficient visible-light-driven photocatalytic hydrogen production on Cu_7S_4/$Zn_{0.2}Cd_{0.8}S$ p-n binary heterojunctions. *Int. J. Hydrogen Energy* **2023**, *48*, 2171–2185. [CrossRef]
38. Wang, Q.; Domen, K. Particulate Photocatalysts for Light-Driven Water Splitting: Mechanisms, Challenges, and Design Strategies. *Chem. Rev.* **2020**, *120*, 919–985. [CrossRef]
39. Li, S.; Wang, C.; Cai, M.; Yang, F.; Liu, Y.; Chen, J.; Zhang, P.; Li, X.; Chen, X. Facile fabrication of TaON/Bi_2MoO_6 core-shell S-scheme heterojunction nanofibers for boosting visible-light catalytic levofloxacin degradation and Cr(VI) reduction. *Chem. Eng. J.* **2022**, *428*, 131158. [CrossRef]
40. Sun, Y.; Zhao, Z.; Zhang, W.; Gao, C.; Zhang, Y.; Dong, F. Plasmonic Bi metal as cocatalyst and photocatalyst: The case of Bi/$(BiO)_2CO_3$ and Bi particles. *J. Colloid Interface Sci.* **2017**, *485*, 1–10. [CrossRef] [PubMed]
41. Zhang, D.; Wu, M.; Hao, J.; Zheng, S.; Yang, Y.; Yao, T.; Wang, Y. Construction of Z-scheme heterojunction by coupling $Bi_2Sn_2O_7$ and BiOBr with abundant oxygen vacancies: Enhanced photodegradation performance and mechanism insight. *J. Colloid Interface Sci.* **2022**, *612*, 550–561. [CrossRef]
42. Yin, N.; Chen, H.; Yuan, X.; Zhang, Y.; Zhang, M.; Guo, J.; Zhang, Y.; Qiao, L.; Liu, M.; Song, K. Highly efficient photocatalytic degradation of norfloxacin via $Bi_2Sn_2O_7$/PDIH Z-scheme heterojunction: Influence and mechanism. *J. Hazard. Mater.* **2022**, *436*, 129317. [CrossRef]
43. Zhang, P.; Wang, T.; Chang, X.; Gong, J. Effective Charge Carrier Utilization in Photocatalytic Conversions. *Acc. Chem. Res.* **2016**, *49*, 911–921. [CrossRef]
44. Zhang, T.; Qin, C.; Zhong, J.; Li, J.; Huang, S. In-situ fabrication of Bi^0/$BiVO_4$ photocatalysts with boosted photocatalytic activity. *Mater. Lett.* **2022**, *306*, 130802. [CrossRef]
45. Wang, R.; Zhu, P.; Liu, M.; Xu, J.; Duan, M.; Luo, D. Synthesis and characterization of magnetic $ZnFe_2O_4$/Bi^0-Bi_2MoO_6 with Z-scheme heterojunction for antibiotics degradation under visible light. *Sep. Purif. Technol.* **2021**, *277*, 119339. [CrossRef]
46. Tan, S.T.; Lim, F.S.; Lee, W.J.; Lee, H.B.; Hong, K.J.; Oleiwi, H.F.; Chang, W.S.; Yap, C.C.; Jumali, M.H.H. Rational design of ordered Bi/ZnO nanorod arrays: Surface modification, optical energy band alteration and switchable wettability study. *J. Mater. Res. Technol.-JMR&T* **2021**, *15*, 5213–5220.
47. Chen, Q.; Long, H.; Chen, M.; Rao, Y.; Li, X.; Huang, Y. In situ construction of biocompatible Z-scheme α-Bi_2O_3/$CuBi_2O_4$ heterojunction for NO removal under visible light. *Appl. Catal. B-Environ.* **2020**, *272*, 119008. [CrossRef]
48. Liu, J.; Li, Y.; Li, Z.; Ke, J.; Xiao, H.; Hou, Y. In situ growing of Bi/$Bi_2O_2CO_3$ on Bi_2WO_6 nanosheets for improved photocatalytic performance. *Catal. Today* **2018**, *314*, 2–9. [CrossRef]
49. Li, X.; Zhang, W.; Li, J.; Jiang, G.; Zhou, Y.; Lee, S.; Dong, F. Transformation pathway and toxic intermediates inhibition of photocatalytic NO removal on designed Bi metal@defective $Bi_2O_2SiO_3$. *Appl. Catal. B-Environ.* **2019**, *241*, 187–195. [CrossRef]
50. Wu, C.; Zhou, C.; Chen, Y.; Peng, Z.; Yang, J.; Zhang, Y. Simple Fabrication of Visible Light-Responsive Bi-BiOBr/$BiPO_4$ Heterostructure with Enhanced Photocatalytic Activity. *J. Nanomater.* **2021**, *2021*, 931–943. [CrossRef]